

ADVANCED MATERIALS

Supporting Information

for *Adv. Mater.*, DOI: 10.1002/adma.201905099

High-Performance Thermally Conductive Phase Change
Composites by Large-Size Oriented Graphite Sheets
for Scalable Thermal Energy Harvesting

Si Wu, Tingxian Li, Zhen Tong, Jingwei Chao, Tianyao Zhai,
Jiaxing Xu, Taisen Yan, Minqiang Wu, Zhenyuan Xu, Hua
Bao, Tao Deng,* and Ruzhu Wang**

Supporting Information

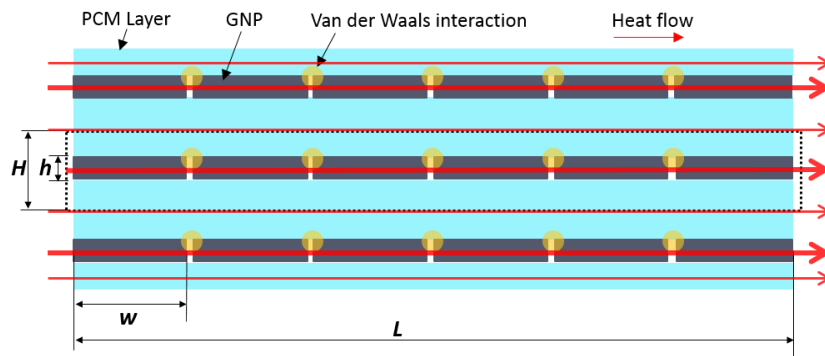
High-Performance Thermally Conductive Phase Change Composites by Large-Size Oriented Graphite Sheets for Scalable Thermal Energy Harvesting

Si Wu, Tingxian Li, Zhen Tong, Jingwei Chao, Tianyao Zhai, Jiaying Xu, Taisen Yan, Minqiang Wu, Zhenyuan Xu, Hua Bao, Tao Deng*, and Ruzhu Wang**

Supplementary Texts

Conceptual design of layered phase change composites (PCCs) with maximum in-plane TCE

An extreme case where graphite sheets and PCM layer form separate thermally conductive pathways in the direction along with the aligned sheets (in-plane) inside the composites is demonstrated below. This parallel configuration makes the heat conduction conform to the parallel model of thermal transport so as to maximize the contribution of GNPs to TCE in theory.



Here, the parallel model can be expressed as follows:

$$K_{\text{comp, in-plane}} = \phi K_{\text{sheet}} + (1 - \phi) K_{\text{PCM}} = \frac{h}{H} K_{\text{sheet}} + \left(1 - \frac{h}{H}\right) K_{\text{PCM}} \quad (1)$$

where $K_{\text{comp, in-plane}}$ is the effective in-plane thermal conductivity of PCCs, K_{sheet} the thermal conductivity of graphite sheet, K_{PCM} the thermal conductivity of PCM, ϕ the volume fraction of graphite sheet, h is the thickness of single sheet and H is the total thickness of single sheet and its PCM coating.

For an individual long graphite sheet, its thermal resistance (R_{sheet}) can be calculated:

$$R_{\text{sheet}} = \left(\frac{L}{w} - 1\right) R_{\text{g/g}} + \frac{L}{w} \frac{w}{K_{\text{g}}} \quad (2)$$

where L is the length of sheet and w is the length of individual GNP. The first item in the right hand is the total interface thermal resistance between adjacent GNPs and the second is the total thermal resistance of GNP itself. Then its effective thermal conductivity (K_{sheet}) can be expressed as:

$$K_{\text{sheet}} = \frac{L}{R_{\text{sheet}}} = \frac{L}{\left(\frac{L}{w} - 1\right)R_{\text{g/g}} + \frac{L}{w} \frac{w}{K_g}} = \frac{1}{\frac{R_{\text{g/g}}}{w} - \frac{R_{\text{g/g}}}{L} + \frac{1}{K_g}} \quad (3)$$

Ideally, at the order of magnitude level, $w \sim 10^{-6} \text{ m}$, $L \geq 10^{-3} \text{ m}$, $K_g \sim 10^3 \text{ W m}^{-1} \text{ K}^{-1}$ and $R_{\text{g/g}} \sim 10^{-9} \text{ m}^2 \text{ K W}^{-1}$,^[1,2] then one can obtain the $\frac{R_{\text{g/g}}}{w} \sim 10^{-3} \text{ m K W}^{-1}$, $\frac{R_{\text{g/g}}}{L} < 10^{-6} \text{ m K W}^{-1}$, and

$\frac{1}{K_g} \sim 10^{-3} \text{ m K W}^{-1}$. Obviously, $\frac{R_{\text{g/g}}}{L} \ll \frac{1}{K_g} \sim \frac{R_{\text{g/g}}}{w}$. Therefore, the item $\frac{R_{\text{g/g}}}{L}$ can be ignored and

K_{sheet} can be expressed as:

$$K_{\text{sheet}} = \frac{1}{\left(\frac{1}{w}\right)R_{\text{g/g}} + \frac{1}{K_g}} \quad (4)$$

The value of K_{sheet} can be up to the order of magnitude of $10^3 \text{ W m}^{-1} \text{ K}^{-1}$. $1/w$ can be defined as the in-plane spatial density of vdW interface. This indicates that the thermally conductive pathway constituted of vdW-bonding GNPs has ultrahigh thermal conductivity, which would contribute to very high TCE even though the graphite sheets are at low volume fraction.

Calculation models of effective thermal conductivity of PCCs

In order to theoretically calculate the effective thermal conductivity, two key parameters need to be firstly determined, the volume fraction of filler and the effective thermal conductivity of filler. In this work, the volume of composite block consists of three parts: GNPs, PCM and pores. It should be noted that the packed densities of composite blocks are controlled near the leakage alarm density and there are some pores existing in the composite block.

$$V_{\text{Com}} = V_{\text{PCM}} + V_{\text{GNP}} + V_{\text{pore}} \quad (5)$$

To simplify the analysis, the filler can be considered as the combination of GNPs and pores:

$$V_{\text{Filler}} = V_{\text{GNP}} + V_{\text{pore}} \quad (6)$$

The volume fraction (ϕ) of fillers in the WEG-based composites and 15-WEG-based composites can be calculated as follows:

$$\phi = \frac{V_{\text{Com}} - V_{\text{PCM}}}{V_{\text{Com}}} = \frac{V_{\text{Filler}}}{V_{\text{Com}}}, \quad (V_{\text{Filler}} = V_{\text{C-WEG}}, \text{ or } V_{\text{C-15-WEG}}) \quad (7)$$

The volume fraction of fillers can also be derived from the packed density of composite block (ρ_{Com}), mass fraction of filler(φ_{wt}), and density of SA ($\rho_{\text{PCM},s}$):

$$\phi = 1 - \frac{(1 - \varphi_{\text{wt}})\rho_{\text{Com}}}{\rho_{\text{PCM},s}} \quad (8)$$

Then, the effective density of fillers (WEG or 15-WEG) can be denoted:

$$\rho_{\text{Filler}} = \frac{m_{\text{Filler}}}{V_{\text{Com}} - V_{\text{PCM}}}, \quad (\rho_{\text{Filler}} = \rho_{\text{C-WEG}}, \text{ or } \rho_{\text{C-15-WEG}}) \quad (9)$$

which can also be calculated from the packed density of composite block (ρ_{Com}), mass fraction of filler(φ_{wt}), and density of SA ($\rho_{\text{PCM},s}$):

$$\rho_{\text{Filler}} = \frac{\rho_{\text{Com}}\varphi_{\text{wt}}}{1 - \frac{(1 - \varphi_{\text{wt}})\rho_{\text{Com}}}{\rho_{\text{PCM},s}}} \quad (10)$$

Generally, the effective thermal conductivity of composites can be predicted by classical theoretical model based on effective media approach (EMA). The equations of frequently-used theoretical models are summarized in Table S2.

The effective thermal conductivity of laminated composites whose fillers have a large aspect ratio can be predicted by the ‘‘Laminated model’’ derived from Nan’s model (Table S2). Based on the assumptions with a large aspect ratio (idea case, $L_{11}=L_{22}=0, L_{33}=1$), the effective thermal conductivities of Laminated model equations reduce to: ^[5]

$$K_{\text{eff}}^{11} = K_{\text{eff}}^{22} = K_{\text{m}} \frac{2 + \phi \left[\frac{K_{\text{f}}}{K_{\text{m}}} (1 + \langle \cos^2 \theta \rangle) \right]}{2 - \phi \left[\frac{K_{\text{f}}h - K_{\text{m}}h - R_{\text{bd}}K_{\text{f}}K_{\text{m}}}{K_{\text{f}}h} (1 - \langle \cos^2 \theta \rangle) \right]} \quad (11)$$

$$K_{\text{eff}}^{33} = K_m \frac{1 + \phi \left[\frac{K_f}{K_m} (1 - \langle \cos^2 \theta \rangle) \right]}{1 - \phi \left[\frac{K_f h}{h + R_{\text{bd}} K_f \langle \cos^2 \theta \rangle} \right]} \quad (12)$$

where θ is the angle between the materials axis x_3 and the local filler symmetric axis, h is the thickness of the laminated fillers, and R_{bd} is interfacial thermal resistance between matrix and fillers. Here, we only consider the K_{eff}^{11} and it is referred to the in-plane thermal conductivity in our work. Actually, the parallel model is just an extreme case of laminated model where the θ is equal to 0°

In order to make a comprehensive understanding of the heat transfer in the graphite sheet filled in PCCs (WEG/SA and 15-WEG/SA composites), the effective thermal conductivities of these composites are calculated using the theoretical models in Table S2. The following parameters are given and assumptions are made: (1) PCM is the matrix material with $K_m = 0.18 \text{ W m}^{-1} \text{ K}^{-1}$; (2) the thermal conductivity of filler are referred to the compressed WEG blocks and 15-WEG blocks. The effective density of fillers in the PCCs are calculated as mentioned above.; (3) assuming the GNPs in WEG-based composites and 15-WEG-based composites are highly oriented along the in-plane direction with θ from 0° to 30° ; (4) the value of h is in the range between 100 nm and 400 nm based on our experimental measurements; (5) the values of R_{bd} with $7.7 \times 10^{-8} \text{ K m}^2 \text{ W}^{-1}$ and $11.9 \times 10^{-6} \text{ K m}^2 \text{ W}^{-1}$ are referred to Ref. [5,8], which correspond to the direct GNP-GNP contact and GNP-matrix contact, respectively. Finally, the comparison between experimental and calculated results is shown in Figure S9. Parameters for theoretical calculation of in-plane thermal conductivity are given in Table S3.

From Figure S9a, it can be found that the parallel model predictions agree well with the experimental values, which indicates the heat flow pathways form in the WEG/SA composites system. However, in 15-WEG/SA composites system, the laminated model predictions match

well with the experimental values, especially when $h=100\text{nm}$, $R_{\text{bd}} = 11.9 \times 10^{-6} \text{ K m}^2 \text{ W}^{-1}$, and $\theta = 30^\circ$ as shown in Figure S9b, which means that the GNPs are lowly oriented and the thermal resistance between GNPs and PCM is very high and predominates the overall thermal resistance.

The fabrication and performance test of high power-density energy harvesting device

A high power-density energy harvesting device integrating the leakage-proof WEG/SA composites and copper tubes was developed for thermal energy storage application. In order to coordinate the alignment of graphite sheets with the heat transfer direction, a mold was designed which could orient the compressing direction of composite block along the axial direction of copper tubes. In addition, this design was also helpful to decrease the contact thermal resistance between composite block and copper tubes owing to the one-pass compression molding (Figure S16a). The high power-density energy harvesting device with size of 440 mm (length) \times 150 mm (width) \times 300 mm (Height) and total mass of 16.87 kg contains 8 copper tubes (inner diameter 10 mm, outside diameter 12 mm and length 480 mm) and PCCs (graphite loading 20 wt% and packed density 900 kg m^{-3}). The designed heat capacity was 1 kWh (Figure S16b). An experimental test system was built to evaluate the performance of the high power-density energy harvesting device. The water at constant temperatures of 85°C and 30°C from two thermostatic water baths was used as heat transfer fluid to supply heat to the thermal storage unit in the charging process and extract heat from it in the discharging process. The practical energy storage density was calculated using the flow mass rate and specific heat capacity of heat transfer fluid and discharging/charging time.

The fabrication of leakage-proof WEG/PW composite block and thermal control device for battery monomer

We used the same method to synthesize the leakage-proof 20 wt% WEG/PW composite block. The industrial paraffin wax with melting point, about 44°C , was used as thermal management material. The thermal properties of paraffin wax and WEG/PW composites were

firstly measured using DSC. Their phase change temperature and enthalpy are demonstrated in Table S6. The measured in-plane thermal conductivity of composite block with graphite loading 20.0 wt±0.1% and packed density 950±20 kg m⁻¹ is 18.1±1.6 W m⁻¹ K⁻¹.

Two commercial 18650 lithium-ion battery monomers had same working parameters, including rated capacity 2600 mAh, rated voltage 3.7 V, maximum charging voltage 4.2 V, and minimum discharging voltage 2.5 V. One battery monomer was wrapped with the composite block, and the other was exposed to ambient. The size of battery monomers and composite block was shown in Figure S17a. The composite block with a hole was firstly fabricated. The diameter of hole was a little higher than that of battery monomer. After inserting the battery monomer into the hole, one could heat the composite block to make the paraffin wax melt and then compress the composite block again at appropriate pressure in a mould so as to ensure compact contact between composite block and battery monomer. The compression direction is along the axial direction of battery. The packed density of composite block was 950±20 kg m⁻¹.

The charging/discharging processes of wrapped and non-wrapped battery monomers were kept at same working condition. The ambient temperature was 30 °C. As illustrated in Figure S17c, two monomers were firstly charged at 1.15 C, and then discharged at 2.3 C. The temperatures of two monomers were monitored using the thermal infrared imager. The maximum temperature point of battery monomer was picked and recorded. It was found that the temperatures of wrapped battery monomer increased at lower rate than that of non-wrapped battery monomer in the charging-discharging process. The temperature of non-wrapped battery monomer reached the alarm temperature, 55 °C, before finishing the discharging process. However, the wrapped battery monomer could keep continuous working for several charging/discharging cycles even at higher charging/discharging rate, 3 C. Moreover, the wrapped battery monomer showed higher capacity than the non-wrapped battery monomer due to the lower working temperature.

Supplementary Figures

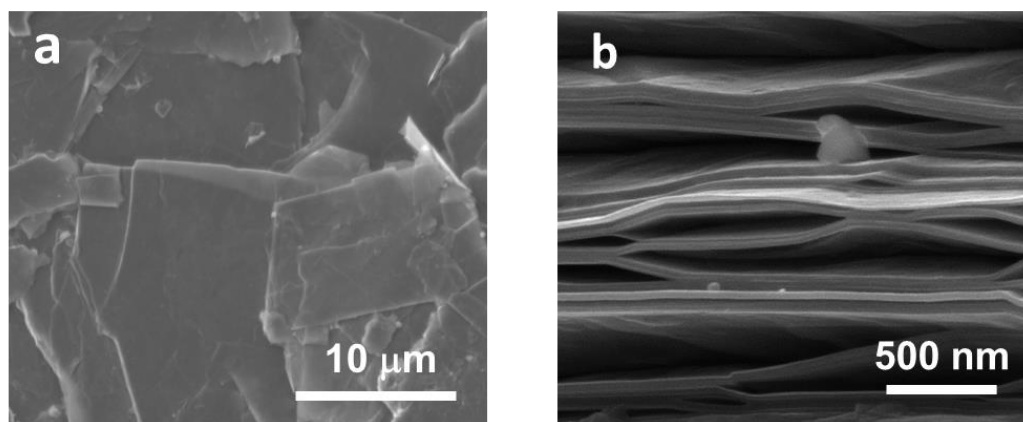


Figure S1. (a) The SEM image of graphite flake at in-plane magnification. It demonstrates that each graphite sheet is constituted of many smaller-size GNPs. (b) Further cross-sectional magnification of graphite intercalation compounds.

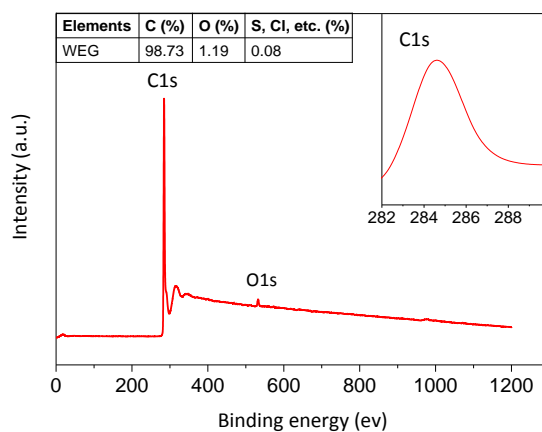


Figure S2. XPS spectra of WEG. The inset curve is C 1s spectrum. The inset table shows the C element content is about 98.7 %.

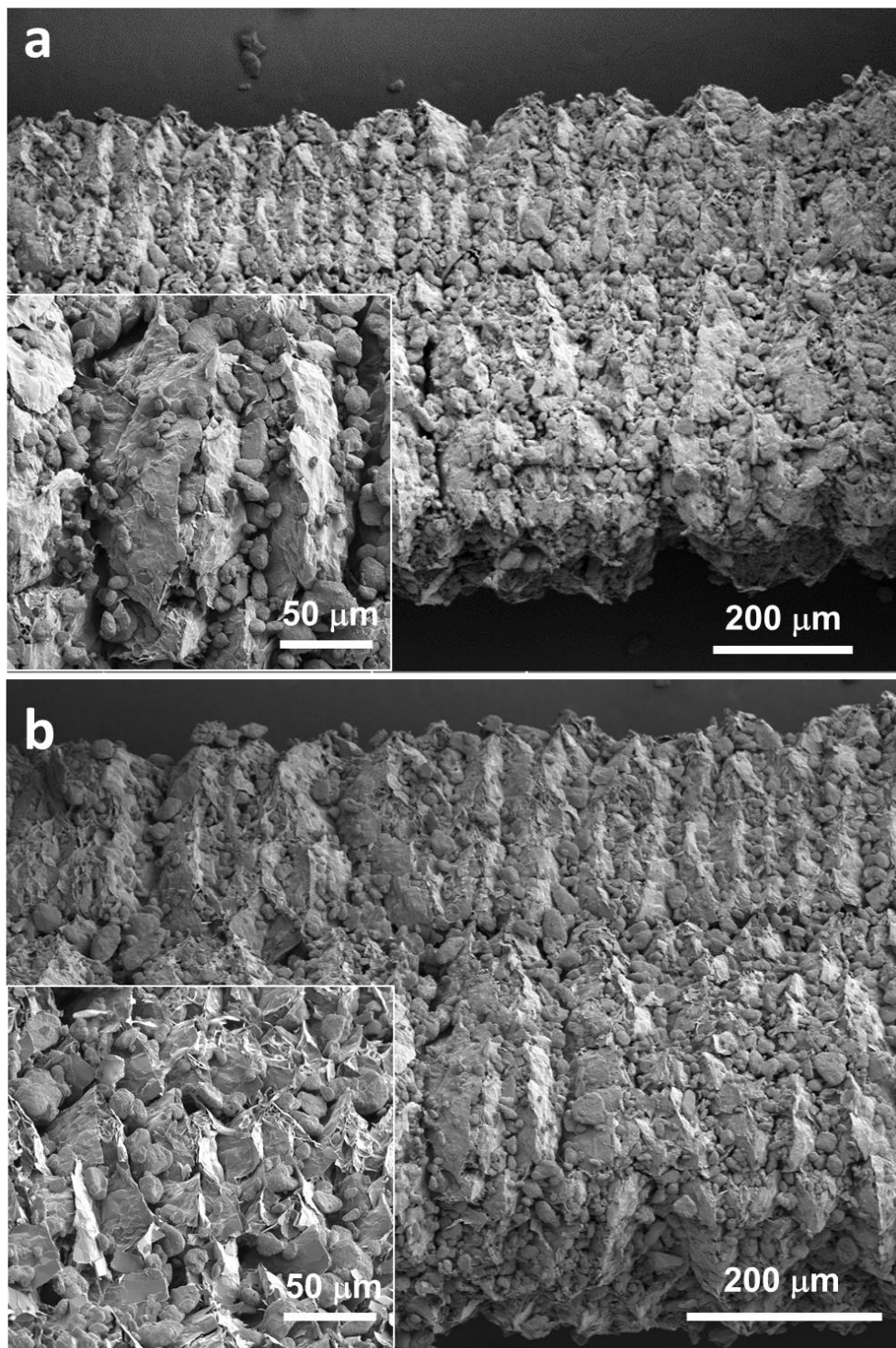


Figure S3. The SEM images of WEG adhered with PCM particles. (a) The SEM image of WEG adhered with SA particles. (b) The SEM image of WEG adhered with PW particles. The insets show the magnified microstructures indicating the size and distribution of PCM particles.

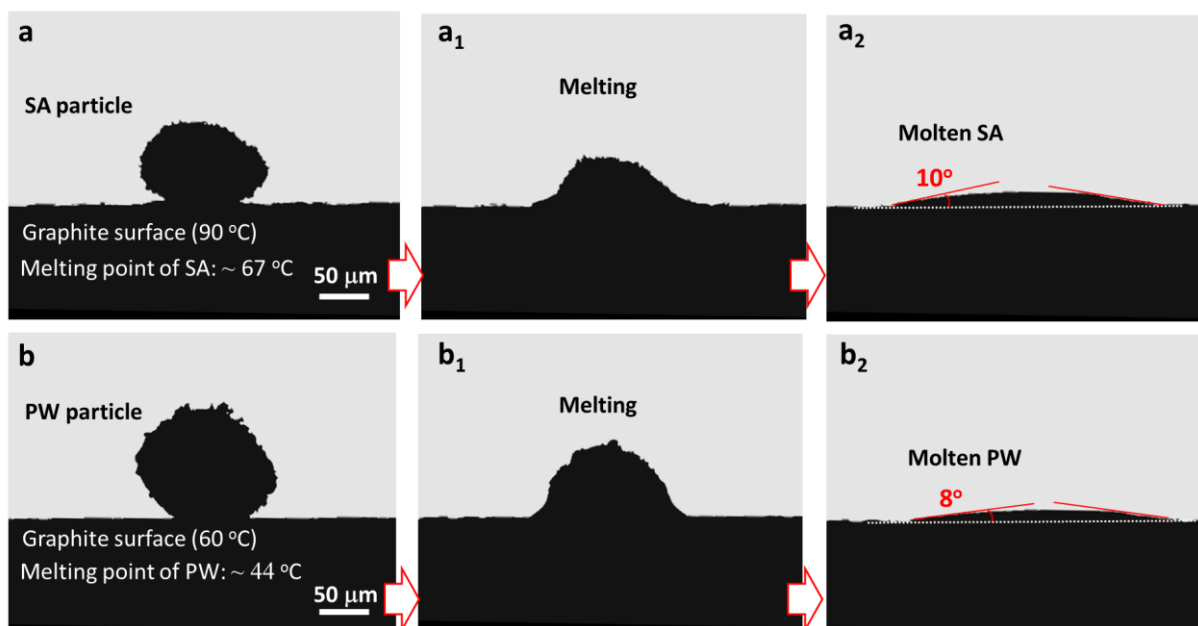


Figure S4. The digital photos of the melting process and contact angle measurement of SA (a) and PW (b) on graphite surface with heat treatment. The compressed WEG block provides the graphite surface. The WEG blocks are placed on a heating plate.

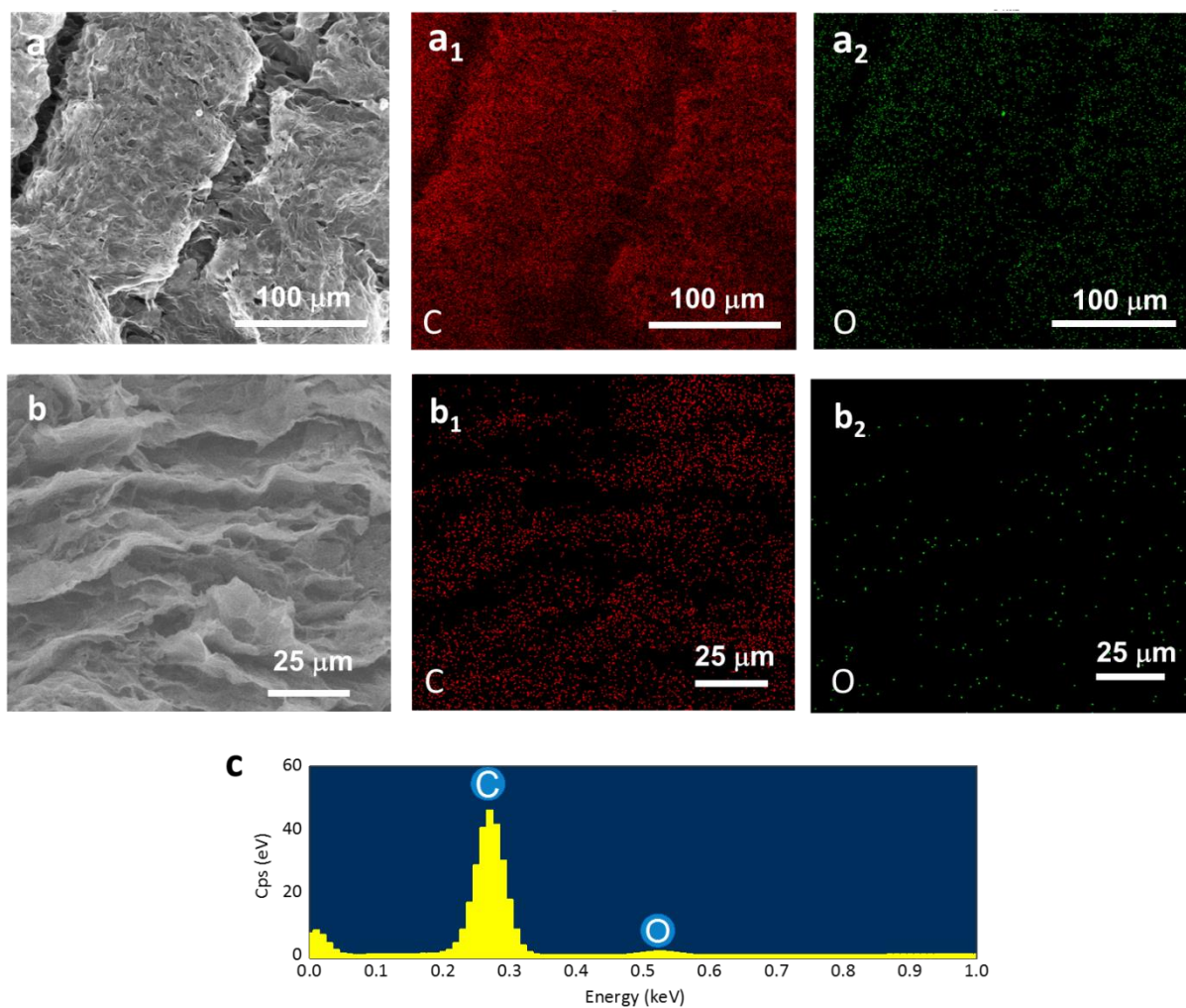


Figure S5. The oxygen and carbon element mappings of WEG with PCM coating and composite block. (a) The SEM image of WEG with SA coating. (a₁) and (a₂) show the carbon (C) element and oxygen (O) element mappings, respectively. (b) The SEM image of composite block. (b₁) and (b₂) show the carbon (C) element and oxygen (O) element mappings, respectively. (c) EDS results of WEG with SA coating. The oxygen mappings reflect the PCM distribution. The graphite loadings of WEG with PCM coating and composite block are 20.0 ± 0.1 wt%.

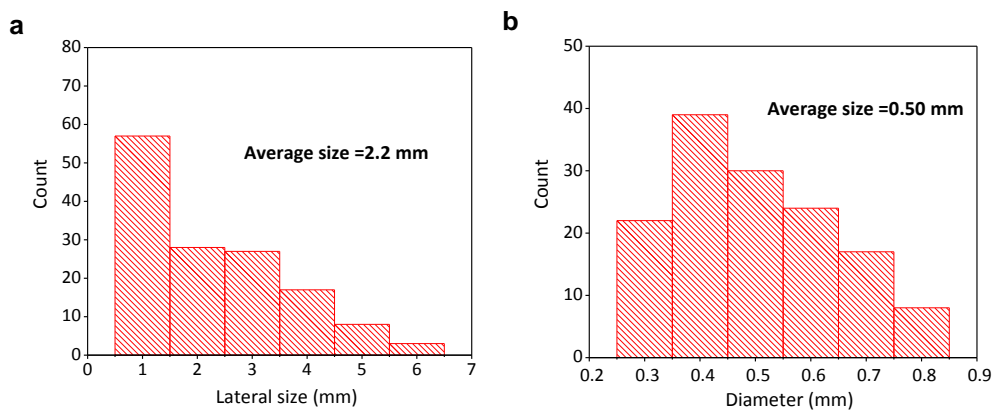


Figure S6. Lateral size (a) and diameter (b) distribution statistics of WEG. WEGs have different intrinsic states including curve and straight. The measurement was performed in their intrinsic states and the maximum length was considered as the effective length of WEG.

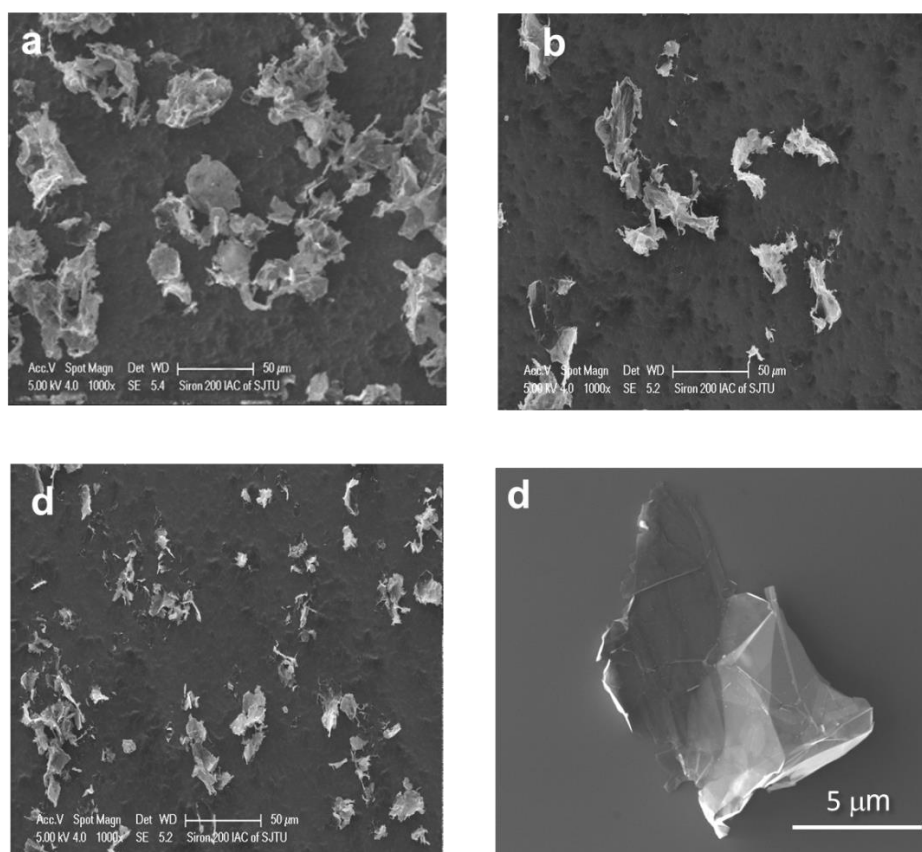


Figure S7. The GNP stacks obtained from ultrasonic process of WEG for 15 min (a), 30 min (b) and 60 min (c). (d) The further magnification of GNP stacks with ultrasonic treatment for 60 min.

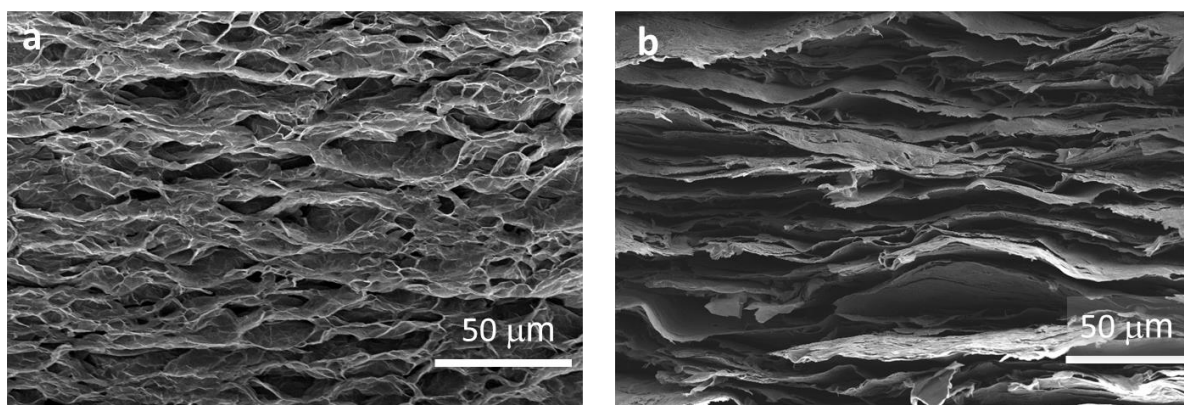


Figure S8. The cross-sectional SEM images of the compressed WEG block at low (a) and high (b) packing density. The highly oriented GNPs are presented at the high packing density.

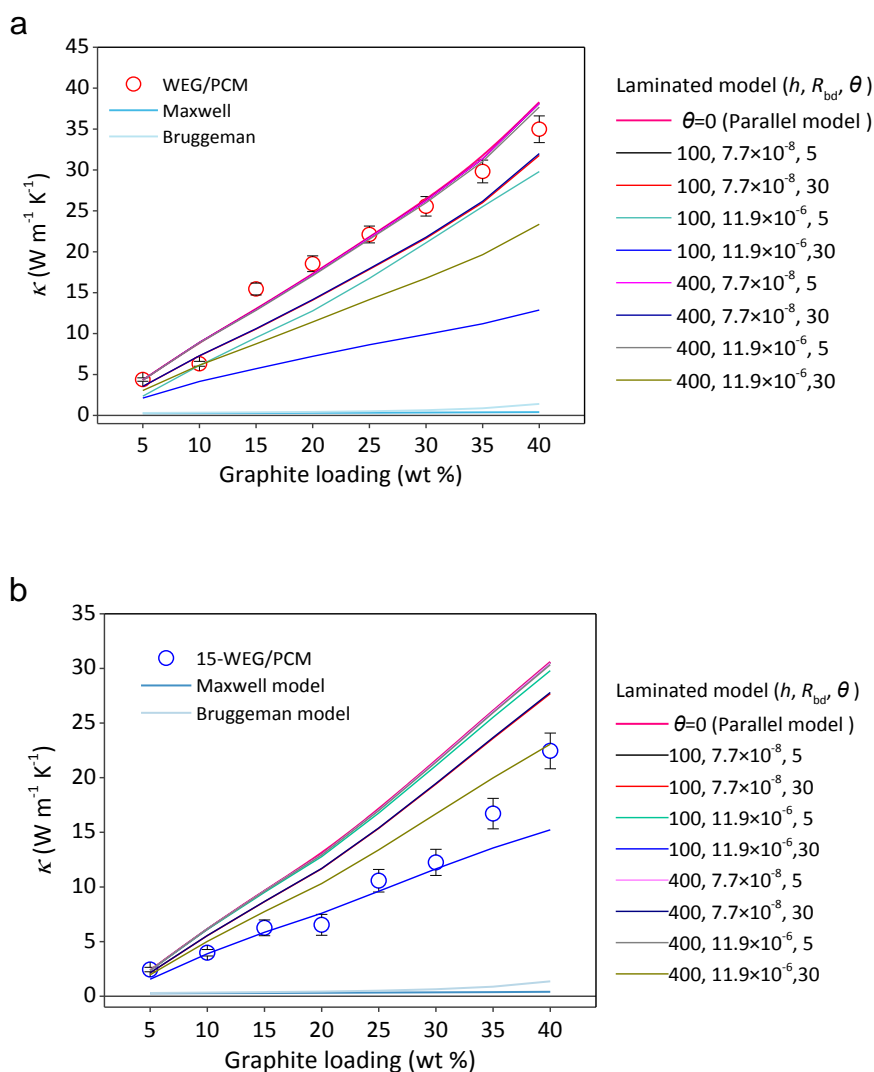


Figure S9. The experimental and calculated in-plane TC of (a) WEG/SA composites and (b) 15-WEG-based composites as functions of graphite loading. The calculation results using parallel model, Maxwell model, Bruggeman model and Laminated model are demonstrated, respectively. For the laminated model, different parameters are chosen to match the experimental values. The GNP thickness h is in unit nm and the interface thermal resistance R_{bd} in unit $\text{K m}^2 \text{W}^{-1}$.

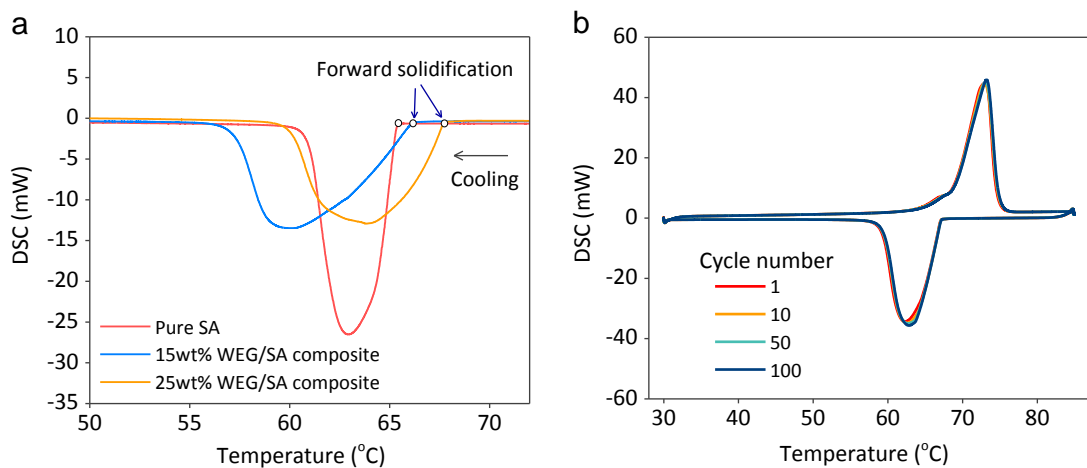


Figure S10. (a) DSC curves of solidification process of pure SA and WEG/SA composites. (b) The cycle stability curves of WEG/SA composites. The heating/cooling rate is $5\text{ }^{\circ}\text{C min}^{-1}$. Their phase change temperatures and heat of fusion are shown in Table S5.

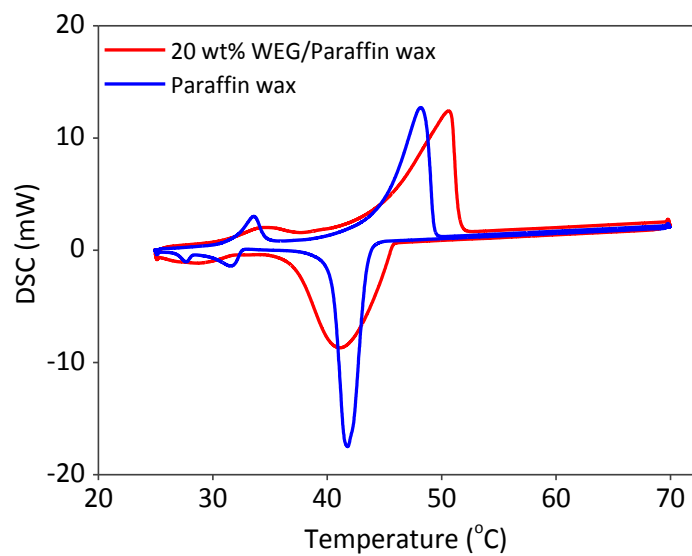


Figure S11. The DSC curves of pure PW and WEG/PW composites. The heating/cooling rate is $5\text{ }^{\circ}\text{C min}^{-1}$. Their phase change temperatures and heat of fusion are shown in Table S6.

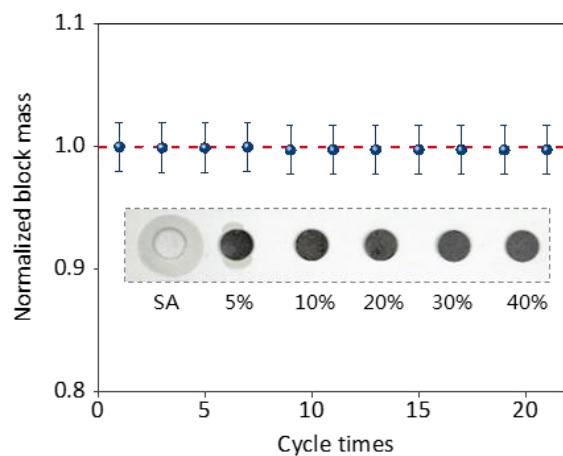


Figure S12. Normalized composite block mass as a function of the melting/solidification cycle number. The measured composite block is at graphite loading 20.0 ± 0.1 wt% and packed density 950 ± 20 kg m⁻³. The inset is the digital photo of pure PCM block and composite blocks during the heat treatment process.

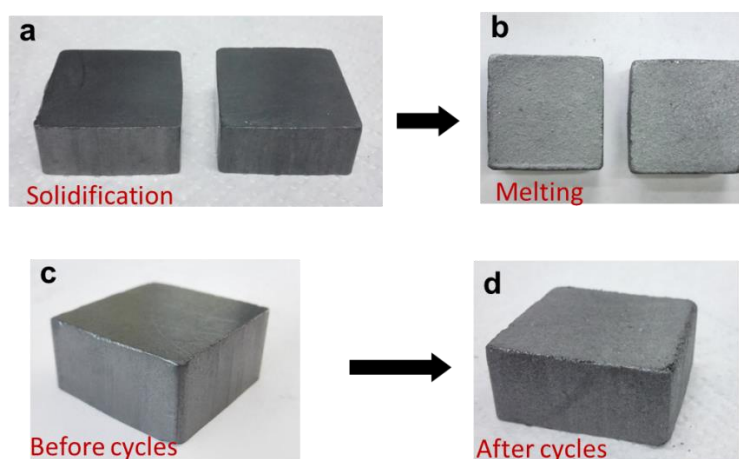


Figure S13. Digital photos of WEG/SA composite blocks before and after melting/solidification cycles. (a) Composite blocks in the solidification state. (b) Composite blocks in the melting state. (c) Composite block before the melting/solidification cycle. (d) Composite block after 100 melting/solidification cycles. The size of composite blocks is 31mm ×31 mm ×14mm. Their graphite loadings are 20.0±0.1 wt% and packed densities are 950±20 kg m⁻³.

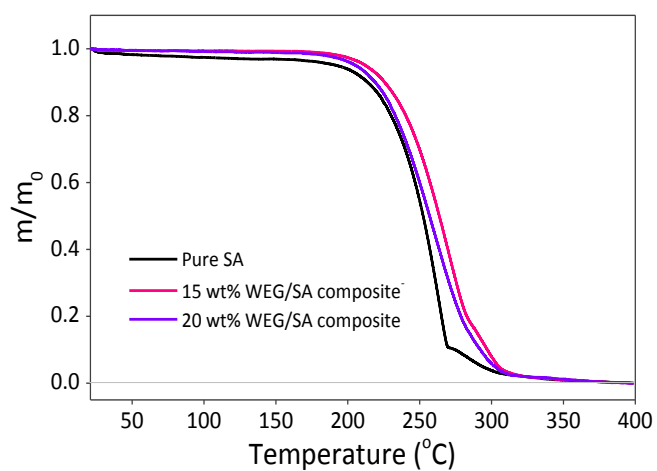


Figure. S14. Thermogravimetric curves of pure SA and WEG/SA composites. The heating/cooling rate is $10\text{ }^{\circ}\text{C min}^{-1}$. m_0 represents the total mass of SA inside composites at room temperature and m represents the residual mass of SA at a certain temperature.

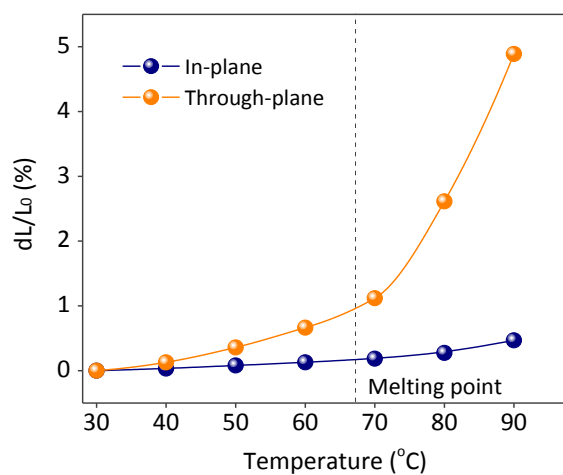


Figure S15. The in-plane and through-plane thermal expansion coefficients of WEG/SA composite block as functions of heat treatment temperature. The composite block is at graphite loading 20.0 ± 0.1 wt% and packed density 950 ± 20 kg m⁻³.

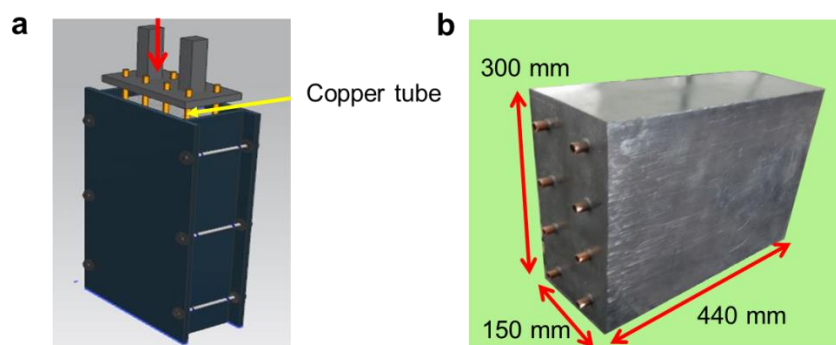


Figure S16. Fabrication and performance test of thermal energy harvesting device with 1 kWh heat capacity. (a) Illustration of the pressure-induced mold for the fabrication of thermal storage module (WEG/SA composites). The red arrow indicates the compression direction. (b) The digital photo of thermal energy harvesting device with 1 kWh heat capacity.

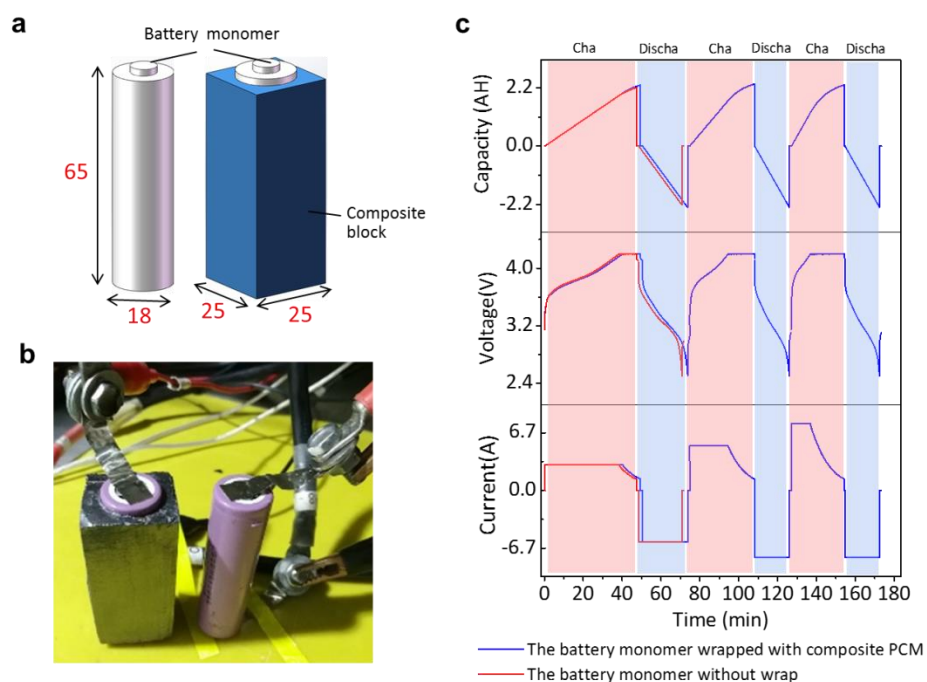


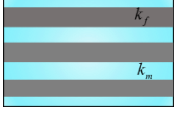
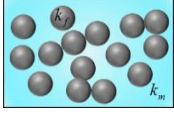
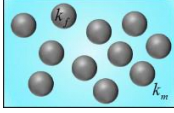
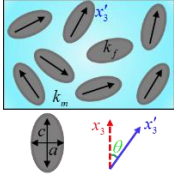
Figure S17. Application of PCCs for battery thermal management. (a) Illustration of two commercial 18650 lithium-ion battery monomer models. The WEG/PW composite block wrapping the battery monomer has graphite loading $20.0\pm 0.1\text{wt}\%$ and packed density $950\pm 20\text{ kg m}^{-3}$. The size is in unit mm. (b) Digital photo of two commercial 18650 lithium-ion battery monomers. (c) The evolution of current, voltage and capacity profiles of two tested battery monomers at different charging/discharging rates.

Supplementary Tables

Table S1. BET specific surface areas and average pore volume of measured samples.

Samples	BET specific surface area ($\text{m}^2 \text{g}^{-1}$)	Average pore volume (cc g^{-1})
WEG	61.9	0.21
40 wt% WEG/SA composites	13.9	0.02278
30 wt% WEG/SA composites	10.7	0.02055
20 wt% WEG/SA composites	5.23	0.01174

Table S2. Four fundamental EMA theoretical models for two-phase materials (assuming the heat flow is in the horizontal direction).

Models	Structure schematic	Effective thermal conductivity equation	Remarks
Parallel ^[6]		$K_{\text{eff}} = \phi K_f + (1 - \phi) K_m$	Heat flow path formed in the filler and matrix respectively.
Maxwell ^[6]		$K_{\text{eff}} = K_m \left[\frac{K_f + 2K_m + 2\phi(K_f - K_m)}{K_f + 2K_m - \phi(K_f - K_m)} \right]$	Particle filler, low volume fraction ($\phi < 25\%$)
Bruggeman ^[7]		$(1 - \phi) \frac{K_m - K_{\text{eff}}}{K_m + 2K_{\text{eff}}} + \phi \frac{K_f - K_{\text{eff}}}{K_f + 2K_{\text{eff}}} = 0$	Particle filler, low volume fraction ($\phi < 40\%$)
Nan ^[6]		$K_{\text{eff}}^{11} = K_{\text{eff}}^{22} = K_m \frac{2 + \phi [\beta_{11}(1 - L_{11})(1 + \langle \cos^2 \theta \rangle) + \beta_{33}(1 - L_{33})(1 - \langle \cos^2 \theta \rangle)]}{2 - \phi [\beta_{11}L_{11}(1 + \langle \cos^2 \theta \rangle) + \beta_{33}L_{33}(1 - \langle \cos^2 \theta \rangle)]} \beta_{ii} = \frac{K_{ii}^c - K_m}{K_m + L_{ii}(K_{ii}^c - K_m)}$ $K_{\text{eff}}^{33} = K_m \frac{1 + \phi [\beta_{11}(1 - L_{11})(1 - \langle \cos^2 \theta \rangle) + \beta_{33}(1 - L_{33})\langle \cos^2 \theta \rangle]}{1 - \phi [\beta_{11}L_{11}(1 - \langle \cos^2 \theta \rangle) + \beta_{33}L_{33}\langle \cos^2 \theta \rangle]}$	L_{ii} and $\cos^2 \theta$ related to geometry

* K_m is the thermal conductivity of matrix, K_f is the thermal conductivity of filler, K_{eff} is the effective thermal conductivity of composites, and ϕ is the volume fraction of filler.

Table S3. Parameters for theoretical calculation of in-plane thermal conductivity of WEG-based composites and 15-WEG-based composites. (The errors are not included)

Sample number	φ_{wt}	ρ_{comp} (kg m^{-3})	$\rho_{C-WEG} = \rho_{C-15-WEG}$ (kg m^{-3})	ϕ	K_{SA} ($\text{W m}^{-1} \text{K}^{-1}$)	K_{C-WEG} ($\text{W m}^{-1} \text{K}^{-1}$)	$K_{C-15-WEG}$ ($\text{W m}^{-1} \text{K}^{-1}$)
1	0.05	875.27	316.36	0.14	0.18	30.20	15.93
2	0.10	904.35	577.63	0.16	0.18	56.20	38.45
3	0.15	935.43	797.04	0.18	0.18	72.90	53.94
4	0.20	968.72	983.92	0.20	0.18	87.00	65.2
5	0.25	1004.48	1144.99	0.22	0.18	98.80	77.2
6	0.30	1042.97	1285.26	0.24	0.18	107.70	87.9
7	0.35	1084.52	1408.51	0.27	0.18	116.40	96.4
8	0.40	1129.53	1517.66	0.30	0.18	128.20	102.2

Table S4. Comparison of thermal conductivity of composites with 2D fillers.

Fillers	PCM/polymer	Filler loading	K_c/K_m (W m ⁻¹ K ⁻¹)	Measurement method	Year and ref.
WEG	Pentaglycerine	4 wt%	0.94/0.23	Laser flash	2018 ^[9]
Graphene	Epoxy resin	10 vol%	5.1/0.2	Laser flash	2012 ^[10]
Graphene	Epoxy resin	10 wt%	1.53/0.2	Laser flash	2013 ^[11]
Graphene	Epoxy resin	45 vol%	11/0.2	Transient plane source	2018 ^[12]
WEG	HDPE	20 wt%	2.25/0.44	Transient plane source	2017 ^[13]
Graphene	Epoxy resin	55 wt%	8/0.2	Laser flash	2019 ^[14]
3D Carbon	PEG8000	35 wt%	0.94/0.28	Transient plane source	2018 ^[15]
GNP	Polycarbonate	20 wt%	7.3/0.24	Transient plane source	2016 ^[16]
Graphene	PVDF	25 vol%	10/0.2	Laser flash	2015 ^[17]
GO	Cellulose	30 wt%	6.17/1.12	Laser flash	2016 ^[18]
rLGO	PVDF-HFP	27.2 wt%	19.5/0.22	Laser flash	2016 ^[19]
GNP	Polyethylene	10 wt%	5.9/0.5	Angstrom	2017 ^[20]
GNP	PDMS	20 vol%	6.05/0.18	Steady state	2016 ^[21]
h-BN	Epoxy resin	9.29 vol%	2.8/0.16	Laser flash	2015 ^[22]
WEG	CBT	20 wt%	6.7/0.3	Transient plane source	2016 ^[23]
WEG	SA	5 wt%	4.4/0.18	Laser flash	this work
WEG	SA	10 wt%	6.3/0.18	Laser flash	this work
WEG	SA	20 wt%	18.5/0.18	Laser flash	this work
WEG	SA	30 wt%	25.6/0.18	Laser flash	this work
WEG	SA	40 wt%	35.0/0.18	Laser flash	this work

Note: 1. K_c represents thermal conductivity of composites and K_m represents thermal conductivity of PCM or polymer; 2. CNT- carbon nanotube, GO-graphene oxide, rLGO- reduced large-area graphene oxide, h-BN- hexagonal boron nitride; 3. The K_c in Ref. [9-15] are the bulk TC and these in Ref. [16-23] and our work are the in-plane TC. 5. The corresponding volume loadings of WEG in our work are given in Table S3.

Table S5. Phase change temperatures and enthalpies of WEG/SA composites at different graphite loadings. (The errors are not included)

Graphite loading (wt%)	Melting temperature (°C)	Melting enthalpy (J g ⁻¹)	Solidification temperature (°C)	Solidification enthalpy (J g ⁻¹)
0	67.22	206.03	65.20	206.01
5	67.41	195.78	66.45	194.70
10	67.22	185.12	66.37	184.07
15	67.84	174.61	66.11	174.45
20	67.58	165.88	65.99	165.17
25	67.89	155.86	67.49	154.41
30	67.76	144.18	67.58	143.16
35	67.95	134.85	67.00	134.76
40	67.73	122.78	67.04	122.72

Table S6. Phase change temperatures and enthalpies of pure paraffin wax and WEG/PW composites. (The errors are not marked)

Graphite loading (wt%)	Melting temperature (°C)	Melting enthalpy (J g ⁻¹)	Solidification temperature (°C)	Solidification enthalpy (J g ⁻¹)
0	44.51	163.74	43.28	159.92
20	44.09	130.10	45.74	132.01

Supplementary References

- [1] X. Shen, Z. Wang, Y. Wu, X. Liu, Y. He, J. Kim, *Nano Lett.* **2016**, *16*, 3585.
- [2] A. A. Balandin, *Nat. Mater.* **2011**, *10*, 569.
- [3] B. Zalba, J. M. Marin, L. F. Cabeza, H. Mehling, *Appl. Therm. Eng.* **2003**, *23*, 251.
- [4] K. Sever, İ. H. Tavman, Y. Seki, A. Turgut, M. Omastova, I. Ozdemir, *Composites Part B: Engineering* **2013**, *53*, 226.
- [5] Q. Li, Y. Guo, W. Li, S. Qiu, C. Zhu, X. Wei, M. Chen, C. Liu, S. Liao, Y. Gong, A. K. Mishra, L. Liu, *Chem. Mater.* **2014**, *26*, 4459.
- [6] J. Ma, C. Nan, *Annu. Rev. Heat Transf.* **2014**, *17*, 303.
- [7] D. A. G. Bruggeman, *Ann. Phys.* **1936**, *417*, 645.
- [8] D. Konatham, D. V. Papavassiliou, A. Striolo, *Chem. Phys. Lett.* **2012**, *527*, 47.
- [9] X. L. G. Z. Ziyuan Wang, *RSC Adv.* **2017**.
- [10] K. M. F. Shahil, A. A. Balandin, *Nano Lett.* **2012**, *12*, 861.
- [11] S. H. Song, K. H. Park, B. H. Kim, Y. W. Choi, G. H. Jun, D. J. Lee, B. Kong, K. Paik, S. Jeon, *Adv. Mater.* **2013**, *25*, 732.
- [12] F. Kargar, Z. Barani, R. Salgado, B. Debnath, J. S. Lewis, E. Aytan, R. K. Lake, A. A. Balandin, *ACS Appl. Mater. Inter.* **2018**, *10*, 37555.
- [13] J. Che, K. Wu, Y. Lin, K. Wang, Q. Fu, *Composites Part A: Applied Science and Manufacturing* **2017**, *99*, 32.
- [14] F. Kargar, Z. Barani, M. Balinskiy, A. S. Magana, J. S. Lewis, A. A. Balandin, *Advanced Electronic Materials* **2019**, *5*, 1800558.
- [15] X. Chen, H. Gao, M. Yang, W. Dong, X. Huang, A. Li, C. Dong, G. Wang, *Nano Energy* **2018**, *49*, 86.
- [16] Y. Yao, X. Zhu, X. Zeng, R. Sun, J. Xu, C. Wong, *ACS Appl. Mater. Inter.* **2018**, *10*, 9669.

- [17] H. Jung, S. Yu, N. Bae, S. M. Cho, R. H. Kim, S. H. Cho, I. Hwang, B. Jeong, J. S. Ryu, J. Hwang, S. M. Hong, C. M. Koo, C. Park, *ACS Appl. Mater. Inter.* **2015**, *7*, 15256.
- [18] N. Song, D. Jiao, P. Ding, S. Cui, S. Tang, L. Shi, *J. Mater. Chem. C* **2016**, *4*, 305.
- [19] P. Kumar, S. Yu, F. Shahzad, S. M. Hong, Y. Kim, C. M. Koo, *Carbon* **2016**, *101*, 120.
- [20] M. Saeidjavash, J. Garg, B. Grady, B. Smith, Z. Li, R. J. Young, F. Tarannum, N. Bel Bekri, *Nanoscale* **2017**, *9*, 12867.
- [21] Y. Guo, Y. Chen, E. Wang, M. Cakmak, *ACS Appl. Mater. Inter.* **2016**, *9*, 919.
- [22] X. Zeng, Y. Yao, Z. Gong, F. Wang, R. Sun, J. Xu, C. Wong, *Small* **2015**, *11*, 6205.
- [23] Y. J. Noh, H. S. Kim, B. Ku, M. Khil, S. Y. Kim, *Adv. Eng. Mater.* **2016**, *18*, 1127.